Title

APPLICATION OF THE MACROSCOPIC AND MICROSCOPIC IMPEDANCE MODELS TO THE ANALYSIS OF THE TOTAL ELECTROCHEMICAL IMPEDANCE OF COPPER DISSOLUTON

Authors

Hauser, A.K
Newman, J.

Publication Date

1989-03-01

LBL-26269
Preprint

Lawrence Berkeley Laboratory
UNIVERSITY OF CALIFORNIA

Materials & Chemical Sciences Division

Submitted to Journal of the Electrochemical Society

Application of the Macroscopic and Microscopic Impedance Models to the Analysis of the Total Electrochemical Impedance of Copper Dissolution

A.K. Hauser and J. Newman

March 1989

Prepared for the U.S. Department of Energy under Contract Number DE-AC03-76SF00098.

DISCLAIMER

LBL-26269

Application of the Macroscopic and Microscopic Impedance Models to the Analysis of the Total Electrochemical Impedance of Copper Dissolution

Alan K. Hauser and John Newman

Department of Chemical Engineering
University of California

and

Materials and Chemical Sciences Division
Lawrence Berkeley Laboratory
One Cyclotron Road
Berkeley, CA 94720

March 21, 1989

LBL-26269

Application of the Macroscopic and Microscopic Impedance Models to the Analysis of the Total Electrochemical Impedance of Copper Dissolution

Alan K. Hauser and John Newman

Department of Chemical Engineering, University of California, and
Materials and Chemical Sciences Division, Lawrence Berkeley Laboratory,
One Cyclotron Road, Berkeley, CA 94720

Abstract

Results of two mathematical models are presented that calculate the frequency response of a copper rotating disk in chloride solutions. Both the macroscopic and microscopic impedance models predict the experimentally observed high-frequency slope that is greater than the 45° convective-diffusion (Warburg) impedance line. The macroscopic impedance model uses concentrated-solution theory, incorporating the Stefan-Maxwell transport equations, to account for multicomponent diffusion, migration, and convection. This model, based on a single overall charge-transfer reaction, predicts impedance curves for the largely mass-transfer controlled anodic dissolution process by using a constant double-layer capacity. Additionally, the electrochemical impedance is analyzed by examining each contribution of the total cell potential and total current giving rise to impedance terms typically neglected in other ac-impedance treatments. The frequency dispersion of the double-layer capacity is accounted for by using the microscopic model of the electrode-electrolyte interface. This lumped-parameter model accounts for (cavity) potential and concentration-dependent charge-transfer reactions, as well as the diffuse and diffusion layers. A three-step (adsorption/electron-transfer/desorption) reaction mechanism is proposed, and the simulated impedance results yield a detailed and quantitative understanding of double-layer adsorption effects. Specifically, insight is gained about the importance and

influence of the many parameters that are used in the microscopic model to characterize the interface but cannot, in general, be independently measured. Thus, an iterative procedure for selecting equilibrium constants and kinetic rate constants is discussed. Additionally, a description of the equilibrated interface is given, including surface-coverage and potential-distribution maps as a function of the supporting electrolyte concentration. Finally, the set of interfacial equilibrium parameters used in the microscopic model is based on a total surface coverage of 0.2%, and the kinetic parameters were selected such that the simulated results agree with the experimental steady-state and impedance data.

1. Introduction

The general Stefan-Maxwell program[1] accounting for multicomponent diffusion, migration, and convection, in addition to any number of homogeneous and heterogeneous reactions, is a powerful algorithm for studying the frequency response of the rotating disk. The model is capable of predicting the total electrochemical impedance based on a constant double-layer capacity, although it is well known[2] that the capacitance of the electrode-electrolyte interface depends on the charge in the compact and diffuse layers. Treatment of the interfacial-reaction processes is necessary to account properly for the accumulation of charge in the electric double layer, and therefore the microscopic model[3] is used to elucidate quantitatively details of this phenomenon. The latter mathematical model accounts for potential and concentration-dependent electron-transfer and desorption/adsorption reactions that occur within the compact region of the double layer. Even though the emphasis of the microscopic model

is on the interfacial reactions, the model also accounts for the diffuse and diffusion layers and ohmic potential losses.

The purpose of this paper is to use the two developed algorithms to describe the current response of a rotating disk to small oscillations around a steady-state potential and to calculate the frequency dependence of the total electrochemical impedance. The simulated results presented here have relevance in the quantitative interpretation of frequency-domain spectroscopic impedance measurements of the dissolution of a copper electrode in 0.1 M HCl.[4] The experimental impedance results are illustrated in figure 1 as function of rotation rate. The microscopic model is used to yield mechanistic information about the reaction processes that were treated simply as a boundary condition in the macroscopic model. Let us next discuss the postulated reaction mechanisms used in the two mathematical models.

The following one-step reaction† represents the overall anodic copper dissolution process and is denoted mechanism I:

$$Cu + 2Cl^- \rightarrow CuCl_2^- + e^- \quad . \tag{1}$$

The modified Butler-Volmer kinetic expression (given in general terms in reference [1]) may be written for reaction 1 as follows:

$$i_f = F k_a' c_{Cl^-,0}^2 \exp\left(\frac{(1-\beta)F}{RT} V\right) - F k_c' c_{CuCl_2^-,0} \exp\left(-\frac{\beta F}{RT} V\right) \quad , \tag{2}$$

† Treatment of this reaction as an EC mechanism has been presented elsewhere,[5] where a chemical (C) reaction follows an electrochemical (E) reaction. Therefore, finite rates of the homogeneous reaction are not considered in this paper.

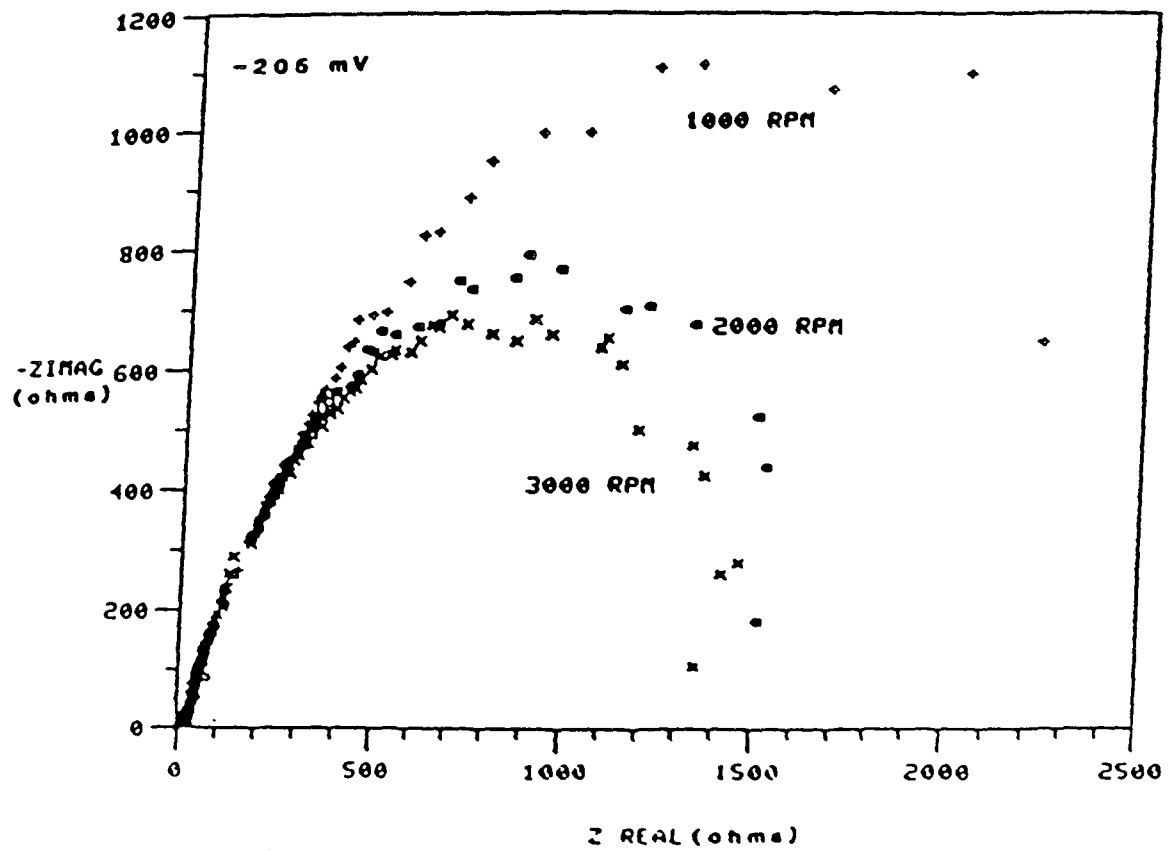

Figure 1. Experimental impedance data (from reference [4]) for copper dissolution in 0.1 N HCl as a function of rotation rate.

provided that the reaction order is proportional to the reaction stoichiometry. $V = \Phi_m - \Phi_0$ is the kinetic potential driving force defined as the potential of the metal electrode relative to a hypothetical reference electrode of a given kind placed just outside the diffuse layer. At equilibrium, the net current density is zero so that equation 2 yields the open-circuit cell potential

$$V_{oc} = \frac{RT}{F} \ln \left(\frac{k_c'}{k_a'} \right) + \frac{RT}{F} \ln \left(\frac{c_{CuCl_2^-,0}}{c^2_{Cl^-,0}} \right) , \tag{3}$$

where $K_c^{(I)} = k_a'/k_c'$ is the equilibrium constant.

A second mechanism for the same anodic copper-dissolution process is possible, where the simple reaction 1 may be written in terms of adsorbed intermediates. Proposed mechanism II is given by the following three reactions:

$$Cl^-_{(OHP)} \rightarrow Cl^-_{(IHP)} \tag{4}$$

$$Cu + 2Cl^-_{(IHP)} \rightarrow CuCl_2^-{}_{(IHP)} + e^- \tag{5}$$

$$CuCl_2^-{}_{(IHP)} \rightarrow CuCl_2^-{}_{(OHP)} \quad . \tag{6}$$

Chloride ions from solution are first specifically adsorbed at the inner Helmholtz plane, where Cl^- can then react electrochemically at the copper electrode. The second step in this mechanism is the one electron-transfer anodic dissolution reaction, where the reactant and the product species remain adsorbed at the surface. The last step of the process is the desorption of the copper chloride complexed species to the outer Helmholtz plane.

A modified form[3] of the Butler-Volmer equation is used to describe the potential and concentration dependence of the electron-transfer reaction (equation 5)

$$i_{e^-,l} = F k_{f,l} \Delta\Gamma \, \Gamma^2_{Cl^-,1} \exp\left(\frac{(1-\beta_l)F}{RT}\Delta\psi_{M-1}\right) - F k_{b,l} \Gamma_{CuCl_2^-,1} (\Delta\Gamma)^2 \exp\left(\frac{-\beta_l F}{RT}\Delta\psi_{M-1}\right) \quad (7)$$

where $\Delta\Gamma = \Gamma_{max} - \Gamma_{Cl^-,1} - \Gamma_{CuCl_2^-,1}$ and $\Delta\psi_{M-1}$ is the cavity potential difference between the metal and the inner Helmholtz plane. Additionally, the kinetic expressions for the potential-dependent desorption/adsorption reactions are given by

$$i_{a,l} = F k_{f,l} \Gamma_{j,1} \exp\left[-(1-\beta_l)\frac{F}{RT}\Delta\psi_{1-2}\right] - F k_{b,l} \Delta\Gamma \, c_{j,2} \exp\left[\beta_l \frac{F}{RT}\Delta\psi_{1-2}\right], \quad (8)$$

where j represents either Cl^- or $CuCl_2^-$ and $\Delta\psi_{1-2}$ is the potential difference between the inner and outer Helmholtz planes. At equilibrium, the rate of each reaction is zero, so that after eliminating the surface concentrations Γ_i from the three equations, the following equilibrium relationship results

$$V_{oc} = \Delta\psi_{ref} + \frac{RT}{F}\ln\left(\frac{K_1^2}{K_2 K_3}\right) + \frac{RT}{F}\ln\left(\frac{c_{CuCl_2^-,0}}{c^2_{Cl^-,0}}\right) . \quad (9)$$

A Boltzmann distribution has been used to describe the potential dependence of the ionic concentrations in the diffuse layer, and the interfacial potential difference V is related to the cavity potentials by $V = \Delta\psi_{M-1} + \Delta\psi_{1-2} + \Delta\psi_{2-0} + \Delta\psi_{ref}$. $\Delta\psi_{ref}$ is a cavity potential difference located at the inner limit of the diffusion layer and will be discussed later.

A one-dimensional model of the electrode-electrolyte interface is shown in figure 2 representing the metal electrode, the compact and diffuse regions of the double layer, and the diffusion layer. The figure illustrates the dependent variables in the microscopic model specifically for reaction mechanism II, where the concentration and potential variables are represented by hexagons. There are three species in the solution ($m = 3$), and one less species is found at the inner Helmholtz plane ($n = 2$). This yields

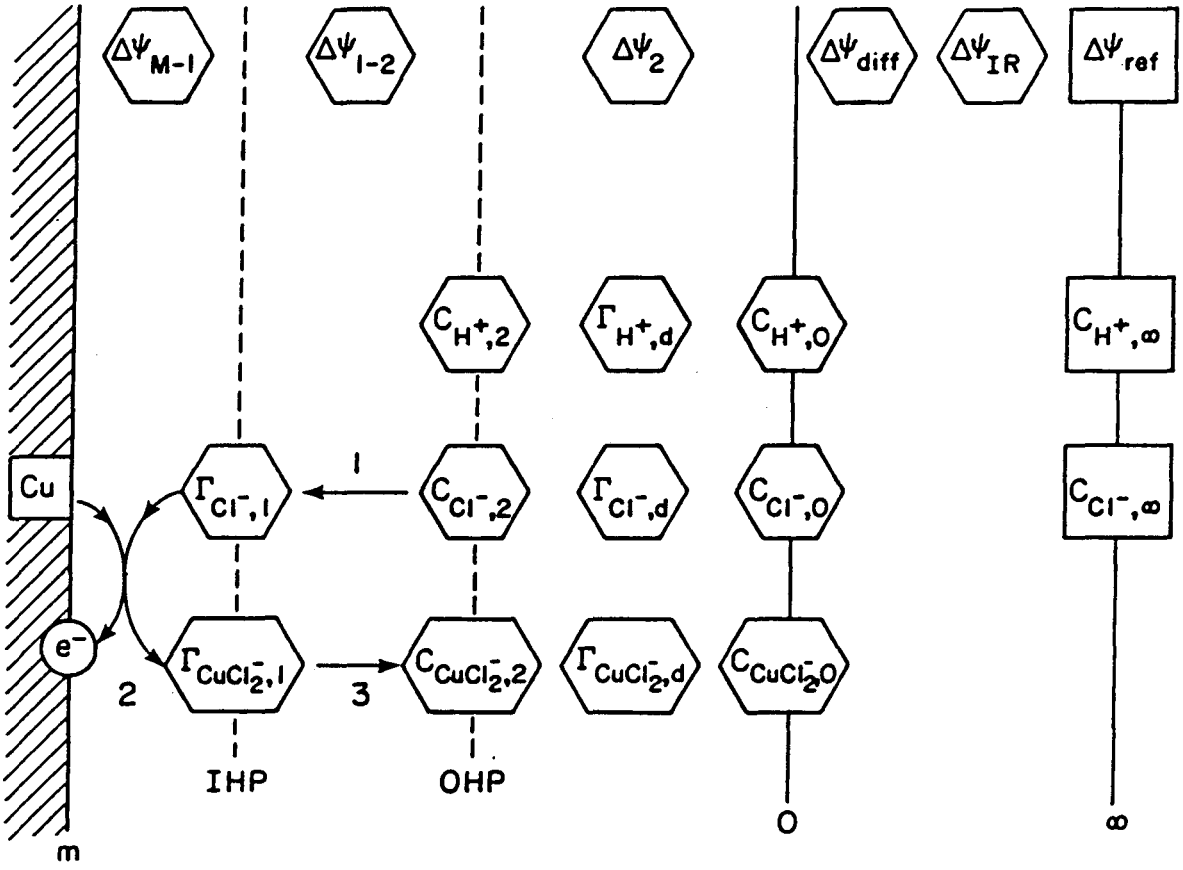

Figure 2. Variables in the microscopic model of the electrode-electrolyte interface when mechanism II is used.

$n + 3m + 5$, or 16, unknowns and equations in the microscopic model. Again, it should be noted that the potential and concentrations are not solved for as continuous functions, as in the macroscopic model, but instead are determined only at the interfacial planes, making the microscopic algorithm a lumped-parameter model. Let us next compare the impedances as calculated by the macroscopic and microscopic models before discussing the system input parameters.

2. Impedances

The impedance of an electrochemical system is defined as ratio of the total alternating potential to the total alternating current, $Z_{tot} = \widetilde{V}_{tot} / \widetilde{i}$. In this section, the electrochemical impedance is analyzed by examining each contribution to the cell potential and current. Two approaches for characterizing the total impedance are taken based upon the expressions given earlier for the current densities. Although the starting point of each is different, both utilize a linear-response analysis.

2.1. Macroscopic Model

The impedance of the copper dissolution process as calculated by the macroscopic model is based on the kinetic expression given by equation 2. Thus, the total cell potential must be expressed in terms of the theoretical kinetic potential difference V. The following expression for the total impedance[1] therefore is used

$$Z_{tot} = \frac{\widetilde{V} + (\widetilde{\Phi}_0 - \widetilde{\Phi}_0)}{\widetilde{i}_f + j\omega\widetilde{q}} + R_\Omega \quad . \tag{10}$$

A schematic of the breakdown of the total impedance used in the Stefan-Maxwell macroscopic model is given in figure 3. Let us next discuss the potentials and currents

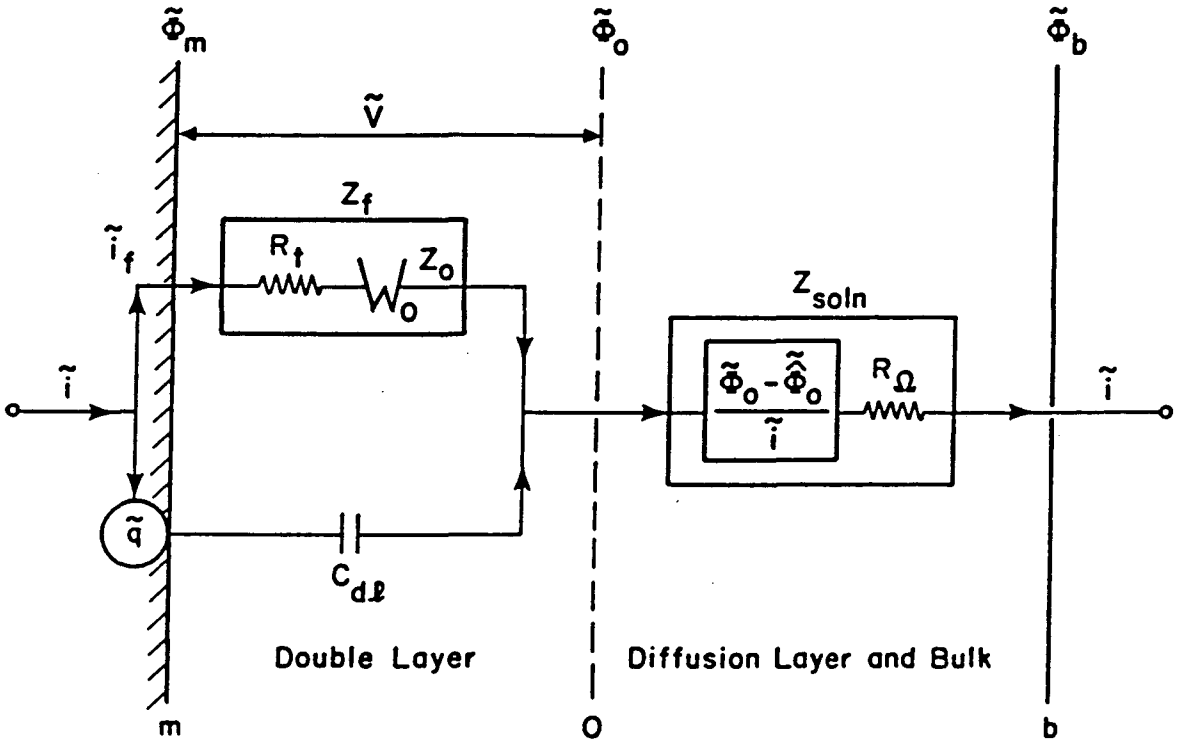

Figure 3. Schematic of the macroscopic model's breakdown of the electrochemical impedance.

illustrated in the figure that contribute to Z_{tot}.

The potential V_{tot} of the metal electrode relative to a reference electrode placed in the bulk consists of three components: $V = \Phi_m - \Phi_0$ is the kinetic driving force across the interface, $\Phi_0 - \hat{\Phi}_0$ is the potential difference across the diffusion layer (and includes the diffusion potential and the ohmic drop due to variations in the conductivity), and the last term in the equation 10, the primary solution resistance R_Ω, gives rise to the ohmic potential drop. It should be noted that Φ_0 is the potential just outside the diffuse part of the double layer, and $\hat{\Phi}_0$ is the potential of the solution adjacent to the working electrode which would be determined by a reference electrode of a given kind if there were no concentration gradients across the boundary layer but the same current distribution prevailed.

The alternating current can pass from the electrode to the solution either by means of faradaic-electrode reactions or by charging the double-layer capacity as illustrated (conceptually) in the figure. This is analogous to the current in a parallel RC circuit, where the capacitor C_{dl} represents the charging of the double layer and the resistor R_t represents the resistance due to the electrochemical reactions. Because the electrode reactions also depend on the concentration of species at the inner limit of the diffusion layer, the resulting mass-transfer component, Z_0, of the faradaic impedance is denoted in the figure with a commonly-used "frequency-dependent" circuit element W_0. Thus, the total electronic-conducting current density $\tilde{i}$ is given by the sum of the alternating faradaic current density, $\tilde{i}_f = \sum_l \tilde{i}_{f,l}$, and the double-layer charging current density, $\tilde{i}_c = j\omega\tilde{q}$. This model uses an idealized view of the electrode-

electrolyte interface, where the charge in the double layer is related to the potential difference across the interface by $\tilde{q} = C_{dl}\tilde{V}$. The double-layer capacity is taken to be a constant, independent of both concentration and potential, such that one might imagine that double-layer charging is due principally to the nonreacting ions of the supporting electrolyte.

Let us now turn our attention to analyzing the components of the total impedance in an attempt to understand better the electrochemical system being studied. This discussion is most useful for clarifying the assumptions that are frequently made in attempts to obtain the faradaic impedance from experimental impedance data. The determination of kinetic parameters and transport properties, *e.g.* the diffusivity, from the faradaic impedance has been disussed previously.[5],[6]

The historically important faradaic impedance is defined by $Z_f = \tilde{V}/\tilde{i}_f$, where one loosely can say that Z_f is obtained from the measured impedance by correcting for the diffusion potential, the ohmic potential drop, and the double-layer capacity. The first two corrections occur in the numerator of equation 10 by using $\tilde{V}$. This means that the diffusion potential, a mass-transfer effect across the boundary layer, is subtracted as well as the ohmic drop; this distinction is seldom (or never) mentioned in the literature. The second correction, for the double-layer capacity, manifests itself in the use of the faradaic current $\tilde{i}_f$, rather than the total current $\tilde{i}$, in the denominator of equation 10. This correction may not be so simple in principle or practice because it presumes that one can distinguish between faradaic current and capacitive current. Frequently the capacitive effect does not overlap the frequency domain of mass-transfer effects, but it must, in general, be expected to overlap the frequency domain of faradaic

effects.

Linearization of the current-density expression (equation 2) and the definition of the faradaic impedance enable the following generalized expression for Z_f to be written[1]

$$Z_f = R_t - R_t \sum_l \sum_i \left(\frac{\partial i_{f,l}}{\partial c_i} \right) \frac{\tilde{c}_{i,0}}{\tilde{i}_f} \quad , \tag{11}$$

where the so called charge-transfer resistance R_t is related to the individual charge-transfer resistances by

$$\frac{1}{R_t} = \sum_l \frac{1}{R_{t,l}} \quad , \quad \text{and} \quad R_{t,l}^{-1} = \left(\frac{\partial i_{f,l}}{\partial V} \right) \quad . \tag{12}$$

Numerical solution of the multicomponent transport equations yields the concentration and the potential profiles adjacent to the rotating disk. From the surface concentrations and the kinetic potential difference, the current and therefore the faradaic impedance can be calculated.

The solution impedance, $Z_{soln} = (\tilde{\Phi}_0 - \tilde{\bar{\Phi}}_0)/\tilde{i} + R_\Omega$, as it will be called, consists of two terms. The first, although typically neglected, results from the establishment of a diffusion potential and ohmic drop (accounting for the variable conductivity) due to concentration variations across the diffusion layer. This effect should be expected to be most significant in concentrated solutions. The second contribution to Z_{soln} is the ohmic resistance out to a reference electrode in the bulk, where conductivity variations are negligible. Assuming a primary current distribution[7] to the rotating disk yields $R_\Omega = \pi r_0 / 4\kappa_\infty$.

2.2. Microscopic Model

The objective of the microscopic model is to account for the frequency dispersion of the double-layer capacity by providing a detailed description of the interfacial-reaction processes. The interfacial kinetic expressions 7 and 8 are written in terms of cavity potential differences within the double layer, and therefore, a different breakdown of the total cell potential is required. The resulting total impedance[3] is given as follows

$$Z_{tot} = \frac{\Delta\tilde{\psi}_{M-1} + \Delta\tilde{\psi}_{1-2} + \Delta\tilde{\psi}_{2-0} + \Delta\tilde{\psi}_{diff}}{\tilde{i}_{e^-} + j\omega\tilde{q}} + R_\Omega \quad , \tag{13}$$

and a schematic illustrating the various terms of Z_{tot} is given in figure 4.

The total alternating current density is seen in the figure to be the sum of the electron-transfer current density, $\tilde{i}_{e^-} = \sum_l \tilde{i}_{e^-,l}$, and the double-layer charging current, $\tilde{i}_c = j\omega\tilde{q}$. The charge can be determined from the following form of Gauss's law

$$\tilde{q} = \frac{\epsilon_{M-1}}{d_{M-1}} \Delta\tilde{\psi}_{M-1} = C_{M-1}\Delta\tilde{\psi}_{M-1} \quad , \tag{14}$$

where $\Delta\tilde{\psi}_{M-1}$ is the potential difference between the metal electrode and the inner Helmholtz plane. The effective capacitance, C_{M-1}, is determined by the permittivity ϵ_{M-1} and the inner-layer thickness d_{M-1}. The electron-transfer reactions are potential and concentration dependent such that the electron-transfer impedance, defined by $Z_{e^-} = \Delta\tilde{\psi}_{M-1} / \tilde{i}_{e^-}$, consists of two components: the electron-transfer resistance, R_{e^-}, and the impedance due to the concentration-dependent reactions, denoted by W_{e^-} in the equivalent circuit. R_{e^-} is the high-frequency limit of Z_{e^-} and is defined by $R_{e^-}^{-1} = \partial i_{e^-}/\partial\Delta\psi_{M-1}$.

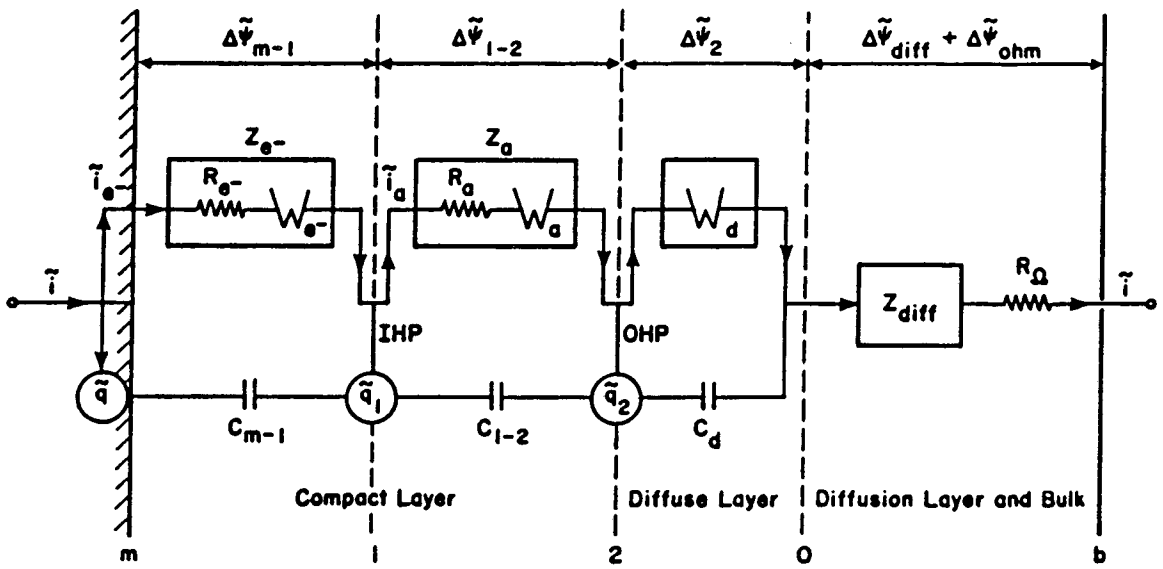

Figure 4. Schematic of the microscopic model's breakdown of the electrochemical impedance.

The double-layer capacity is not taken to be a constant, as was done in the macroscopic model, but instead depends on the charge in the compact ($\widetilde{q}_1 = F\sum_i z_i\widetilde{\Gamma}_{i,1}$) and diffuse ($\widetilde{q}_2 = F\sum_i z_i\widetilde{\Gamma}_{i,d}$) layers. A charge balance on the inner Helmholtz plane yields

$$j\omega\widetilde{q}_1 = \widetilde{i}_{e^-} - \widetilde{i}_a \quad , \tag{15}$$

where $\widetilde{i}_a$ is the alternating current density due to the desorption/adsorption reactions that occur between the IHP and the OHP. These potential and concentration-dependent reactions give rise to the desorption/adsorption impedance, $Z_a = \Delta\widetilde{\psi}_{1-2} / \widetilde{i}_a$, and is the sum of the the kinetic resistance, $R_a^{-1} = \partial i_a/\partial\Delta\psi_{1-2}$, and the frequency-dependent circuit element, W_a. The charge $\widetilde{q}_1$ can be related to C_{M-1} and C_{1-2} by Gauss's law.

A charge balance on the diffuse layer gives

$$j\omega\widetilde{q}_2 = \widetilde{i}_a - \widetilde{i} \quad , \tag{16}$$

where $\widetilde{i}$ is the alternating ionic-conducting current density passed through the electrolyte. The charge $\widetilde{q}_2$ is related to components of the double-lyer capacity by Gauss's law, $\widetilde{q}_2 = -C_{1-2}\Delta\widetilde{\psi}_{1-2}$, and by the definition of the differential diffuse-layer capacity $C_d = -(\partial q_2/\partial\Delta\psi_{2-0})$. The charge balance on the diffuse layer is similar to the material balance

$$j\omega\widetilde{\Gamma}_{i,d} = \widetilde{N}_i^{(1-2)} - \widetilde{N}_i(z=0) \quad , \tag{17}$$

where this conservation equation for each species can be multiplied by Fz_i and summed over all species yielding the current density relationship (equation 16), since $\widetilde{i}_a = F\sum_i z_i\,\widetilde{N}_i^{(1-2)}$. Equation 17 is most useful because one can see that the flux of a

minor species at the inner limit of the diffusion layer[3]

$$\widetilde{N}_i(z=0) = \frac{-D_i}{\delta_i}\frac{d\widetilde{c}_i}{d\xi} = \frac{D_i/\delta_i}{-1/\theta'(0)}\,\widetilde{c}_{i,0} \tag{18}$$

gives rise to an impedance denoted in the figure by W_d, where $-1/\theta'(0) = -\widetilde{c}_{i,0}/\widetilde{c}'_{i,0}$ is the convective-Warburg impedance function for a rotating disk,[8] valid for dilute solutions and no migration. The prime denotes differentiation with respect to $\xi = z/\delta_i$.

The final potential difference in equation 11, and illustrated in the figure 4, is the diffusion potential $\Delta\widetilde{\psi}_{diff}$. Although this potential is typically small for dilute solutions, it is included for completeness. The ohmic potential difference, $\Delta\widetilde{\psi}_{ohm} = \widetilde{i}\,R_\Omega$, is calculated using the bulk solution conductivity κ_∞. The ohmic drop that arises from a variable conductivity due to concentration variations across the diffusion layer is not accounted for, as was done in the macroscopic impedance model. The importance of this omission will be discussed in the results section.

Finally, it is hoped that the discussion here makes it clear that the variation of the impedance with frequency of an electrochemical system *cannot* adequately be accounted for by a finite combination of "true" resistors and capacitors, although it has been customary to do so. The equivalent circuit is included simply to illustrate system behavior qualitatively. It is the interfacial reactions that determine the charge distribution within the double layer, and the charge, $-q = q_1 + q_2$, is a function of the surface concentrations of all species within the double layer as well as the potential. Therefore, to determine the frequency dependence of the electrochemical impedance, it is necessary to solve the lumped-parameter microscopic model numerically for the potentials across the interfacial planes and the surface excesses of all electroactive

species. The current can then be determined from equations 7 and 8, and consequently the total impedance can be calculated using equation 13.

3. Model Parameters

Two mathematical models for the frequency response of a rotating disk electrode have been reviewed. The parameters used in the models to characterize a particular electrochemical system have well-defined physical meaning, but some interfacial parameters are not directly measurable. Let us next present the parameters necessary for the model calculations, including a discussion of the selected values. Bulk transport properties are obtained from the literature; physically-justified values are assumed (and are not adjusted) for the Gauss's law parameters used to describe the charge at the interface; and thermodynamic and kinetic arguments are used to determine the (adjustable) equilibrium and rate constants, respectively.

3.1. Transport Properties

The properties of interest in the electrolytic solution are the bulk-solution ionic concentrations, diffusion coefficients, the electrical conductivity, and the viscosity. Table 1 gives the values of the physical property data corresponding to the copper-dissolution process in 0.1 M HCl at 298.15 K. These parameters are independent of the specific reaction mechanism used in the model and are assumed to be constant.

The bulk conductivity of the electrolytic solution is related to the specified bulk concentrations and mobilities of the charge carrying species by

Table 1. Values of the physical property data for the electrolyte.

species	$D_i \times 10^5$ (cm^2/s)	$c_{i,\infty} \times 10^4$ (mol/cm^3)
Cl^-	2.032	1.0
$CuCl_2^-$	0.568[4]	0.0
H^+	9.312	1.0
$\kappa_\infty = 0.046\ (\Omega \cdot cm)^{-1}$	$\nu = 8.9 \times 10^{-3}\ cm^2/s$	

$$\kappa = \frac{F^2}{RT} \sum_i z_i^2 D_i c_i \quad , \tag{19}$$

where the ionic mobilities have been related to the diffusion coefficients by the Nernst-Einstein relationship $D_i = RTu_i$. The ionic diffusion coefficients at infinite dilution are reported in table 1 as given in reference [9], unless specified otherwise. The viscosity of the infinitely dilute solution at 25 ° C is given by Robinson and Stokes.[10] Additionally, the dielectric permittivity ϵ_{soln} is a property of the electrolytic solution and is given in table 2.

3.2. Gauss's Law Parameters

Table 2 summarizes the physical parameters that are used in Gauss's law to characterize the charge in the double layer. Values are selected for these parameters and are not adjusted.

First, the distances between the interfacial planes are specified, since linear potential profiles are assumed for the lumped-parameter microscopic model. Molecular

Table 2. Physical parameters characteristic of the interfacial double layer.

	(M-1) M→IHP	(1-2) IHP→OHP	(2) OHP→0	(soln) 0→∞
d_j (Å)	1	2	$\lambda = 10^{-7}$ cm	$\overline{\delta} = 1.3\times10^{-3}$ cm
$\epsilon_j \times 10^{12}$ (F/cm)	0.1	0.2	7.0	7.0
C_j (μF/cm^2)	10	10	72	-
$C_{dl} = 5, 10, 30\ \mu\text{F}/\text{cm}^2$				

dimensions of dehydrated and hydrated ions yield values for d_{M-1} and d_{1-2}, respectively. The Debye length λ characterizes the thickness of the diffuse layer and depends on the ionic strength of the solution (0.1 N for the value reported in table 2). The Levich equation gives the Nernst-diffusion-layer thickness $\overline{\delta}$ for a rotation speed of 2000 rpm.

The dielectric permittivity of an infinitely dilute electrolytic solution (and diffuse layer), is obtained by using the relative dielectric constant for water. Within the compact part of the double layer, the electric field is greater than in the solution, and the permittivity is smaller due to dielectric saturation.[9] Close to the surface, oriented water molecules are most aligned yielding the smallest permittivity.

The microscopic integral capacitance, $C_j = \epsilon_j/d_j$ (where j refers to a region within the interface), is calculated using the values of the permittivities and thicknesses given in table 2. Values of the double-layer capacity used in the macroscopic model also are given in the table. The overall differential capacity is defined by $C_{dl} = \partial q/\partial(\psi_M - \psi_0)$ and can be related to the interfacial capacities by

$$\frac{1}{C_{dl}} = \left[\frac{\frac{1}{C_{eff}} - \frac{1}{C_{M-1}} \frac{F}{RT} \bar{q}_1 \left(\frac{1}{C_{1-2}} + \frac{1}{C_d} \right)}{1 - \frac{F}{RT} \bar{q}_1 \left(\frac{1}{C_{1-2}} + \frac{1}{C_d} \right)} \right], \tag{20}$$

where

$$\bar{q} = -F \Delta\Gamma \left(\frac{c_{Cl^-,0}}{K_1} + \frac{c_{CuCl_2^-,0}}{K_3} \right) \exp \left[\frac{F}{RT} (\psi_1 - \psi_0) \right] . \tag{21}$$

An effective capacity for no specific adsorption is given by $1/C_{eff} = 1/C_{M-1} + 1/C_{1-2} + 1/C_d$.

Finally, the available number of sites on the metal surface for reaction is given by $\Gamma_{max} = 10^{-9}$ mol/cm^2. This maximum surface concentration of adsorbed species depends on the sizes and packing relationship of the surface and adsorbate molecules. The value chosen corresponds to 16.6 Å^2/molecule.

3.3. Equilibrium Parameters

The electrode-electrolyte interface is characterized under equilibrium conditions by the "macroscopic" and "microscopic" equilibrium constants, and knowledge of the surface coverage (or adsorption energy of individual ions) would enable the equilibrium constants to be determined. However, thermodynamic data are not available for the adsorbed intermediates in the proposed reaction mechanism II, and the microscopic equilibrium constants must be chosen on some other basis. Additionally, values of the interfacial equilibrium constants cannot be selected independently and are subject to thermodynamic constraints. For example, the open-circuit cell potential, as determined by the microscopic model (equation 9), must be equivalent to the open-circuit potential

given by the macroscopic Nernst equation 3. Thus, depending on the fractional occupation, $\Theta_{i,1} = \Gamma_{i,1}/\Gamma_{max}$, of the adsorbed ions at the inner Helmholtz plane, the set of microscopic equilibrium constants can change, but must remain thermodynamically consistent with the macroscopic equilibrium constant $K_{c,l}$. In this section, a thermodynamic basis for determining the equilibrium constants is described. In the next section, details of the iterative procedure for selecting the specific values for all thermodynamic and kinetic parameters will be discussed.

First, in order to demonstrate the applicability of our stoichiometry accounting method discussed in the previous paper,[3] the stoichiometric coefficients of all the species in mechanism II are given in table 3. Species that appear on the left side of reactions 4, 5, and 6 (when written as an anodic or desorption reaction) have positive stoichiometric coefficients; all products have negative stoichiometric coefficients.

At equilibrium, and in the absence of corrosion, the interfacial reactions have a zero net rate. The charge-transfer equilibrium constants can be determined subsequently as functions of the equilibrium interfacial concentrations and potentials. The equilibrium constant of the electron-transfer reaction 5 is determined from equation

Table 3. Stoichiometric coefficients for species i in reaction l for mechanism II.

rxn	*metal*		*inner Helmholtz plane*		*outer Helmholtz plane*		
l	e^-	Cu	Cl^-	$CuCl_2^-$	Cl^-	H^+	$CuCl_2^-$
1			1		−1		
2	−1	1	2	−1			
3				1			−1

7 by setting $i_{e^-} = 0$, and solving for K_2 yielding

$$K_2^{(II)} = (1 - \sum_j \Theta_{j,1}) \frac{\Theta_{CuCl_2^-,1}}{\Theta_{Cl^-,1}^2} \exp\left(-\frac{F}{RT} \Delta\psi_{M-1}\right) . \tag{22}$$

Again, assuming fast rates of reaction and a Boltzmann distribution, equation 8 yields the equilibrium constant of the desorption/adsorption reactions as follows:

$$K_l^{(II)} = c_{k,0} \frac{1 - \sum_j \Theta_{j,1}}{\Theta_{k,1}} \exp\left[\frac{F}{RT} (\Delta\psi_{1-2} + \Delta\psi_{2-0})\right] . \tag{23}$$

A wealth of information concerning the interfacial properties is incorporated within the three microscopic equilibrium constants. For example, the equations given above for the equilibrated interface can be solved systematically (see figure 5), along with Gauss's law[3] for the IHP and the diffuse layer, to obtain the interfacial potential differences and the surface concentrations of the adsorbed ions in terms of the electrolyte concentration c_{HCl} and the concentration of the minor species $c_{CuCl_2^-,0}$. A schematic summarizing this equilibrium-calculational procedure is given in figure 5. The additional input parameter shown in the figure is the cavity potential difference, $\Delta\psi_{ref} = \psi_0 - \Phi_0$, that relates the quasi-electric potential[9] Φ used in the macroscopic model to the outer or cavity potential ψ used in Gauss's law in the microscopic model. Equating the open-circuit potential equations 3 and 9 yields the constant

$$\Delta\psi_{ref} = -\frac{RT}{F} \ln\left[K_c^{(I)} \frac{K_1^2}{K_2 K_3}\right] \tag{24}$$

in terms of the macroscopic and microscopic equilibrium constants.

The equilibrium constants K_1 and K_3 for the ion-adsorption reactions 4 and 6 provide a measure of the adsorption energy of an ionic species and, therefore, generally

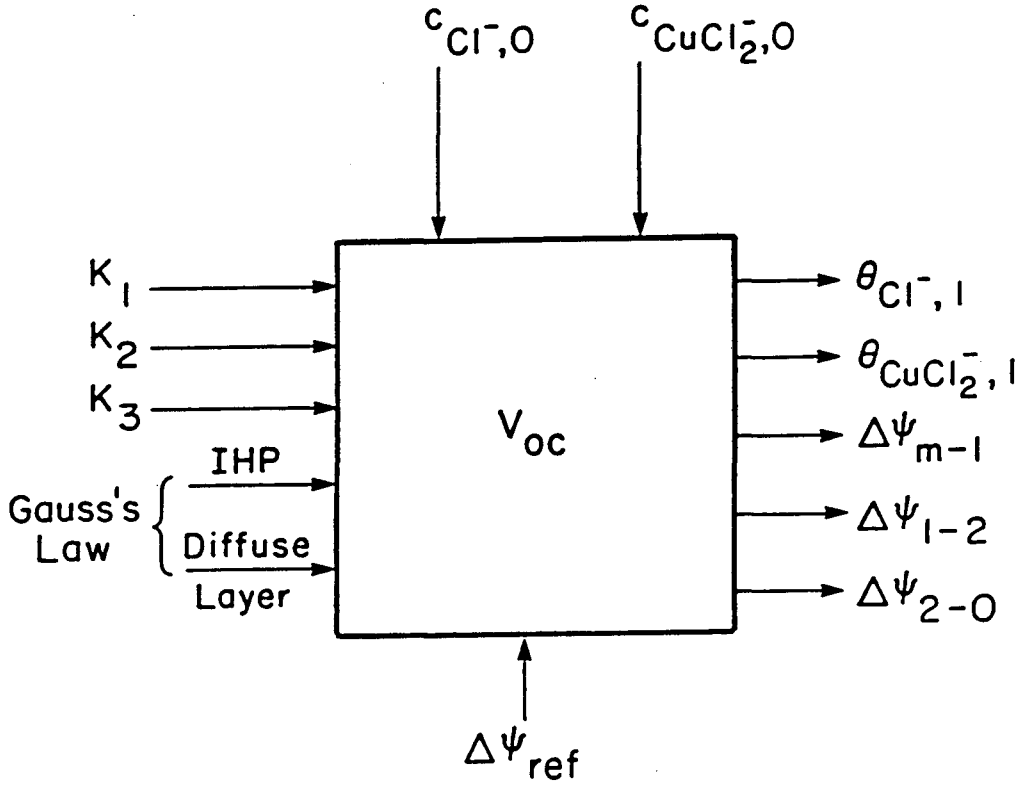

Figure 5. Schematic of the equilibrated-interfacial calculations made in the microscopic model.

determine the level of coverage of the inner Helmholtz plane. One can see this by setting the $\Delta\psi$'s equal to zero in equations 22 and 23 (as a first approximation by ignoring Gauss's law) and selecting reasonable values for the concentrations $c_{Cl^-,0}$ and $c_{CuCl_2^-,0}$. (Results of the steady-state macroscopic model indicate the order of magnitude of the product concentration adjacent to the electrode with consideration of the mass-transfer limitations and the observed current densities.) This calculational procedure is used to determine the following values for the equilibrium constants: $K_1 = 9.98 \times 10^{-2}$ mol/cm^3, $K_2 = 998$, and $K_3 = 3.39 \times 10^{-5}$ mol/cm^3.

Results based on the given set of equilibrium parameters are given in figures 6 and 7. The concentration-distribution map (figure 6) illustrates the thermodynamic relationship between surface coverages and bulk ionic concentrations. Also shown on figure 6 is the result ($\Theta_i = 10^{-3}$ indicated by an open circle) as calculated by the adjustable (within thermodynamic constraints) microscopic equilibrium constants to be used later in the paper. For this case, all charge is assumed to be specifically adsorbed ($q_2 = 0$), and the potential difference, $\Delta\psi_{M-1}$, is related to the charge ($q = -q_1$) adsorbed at the inner Helmholtz plane by Gauss's law (equation 14). A small surface coverage is the basis for this set of adsorption constants because the electrode surface is taken to be sparsely covered.

3.4. Kinetic Parameters

Thermodynamic equilibrium considerations alone cannot be used to determine the distribution of charge within the double layer unless all the interfacial reactions are infinitely fast. When finite rates of the charge-transfer reactions need to be accounted

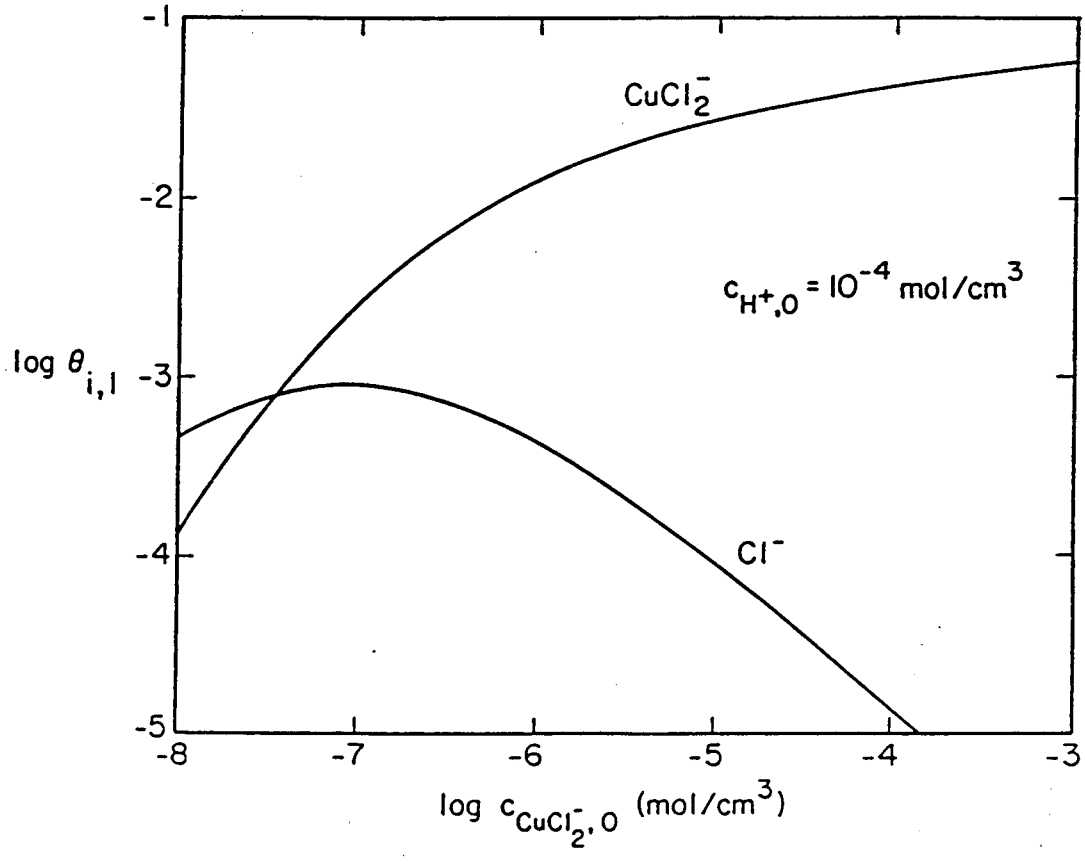

Figure 6. Equilibrated-interfacial concentration-distribution map.

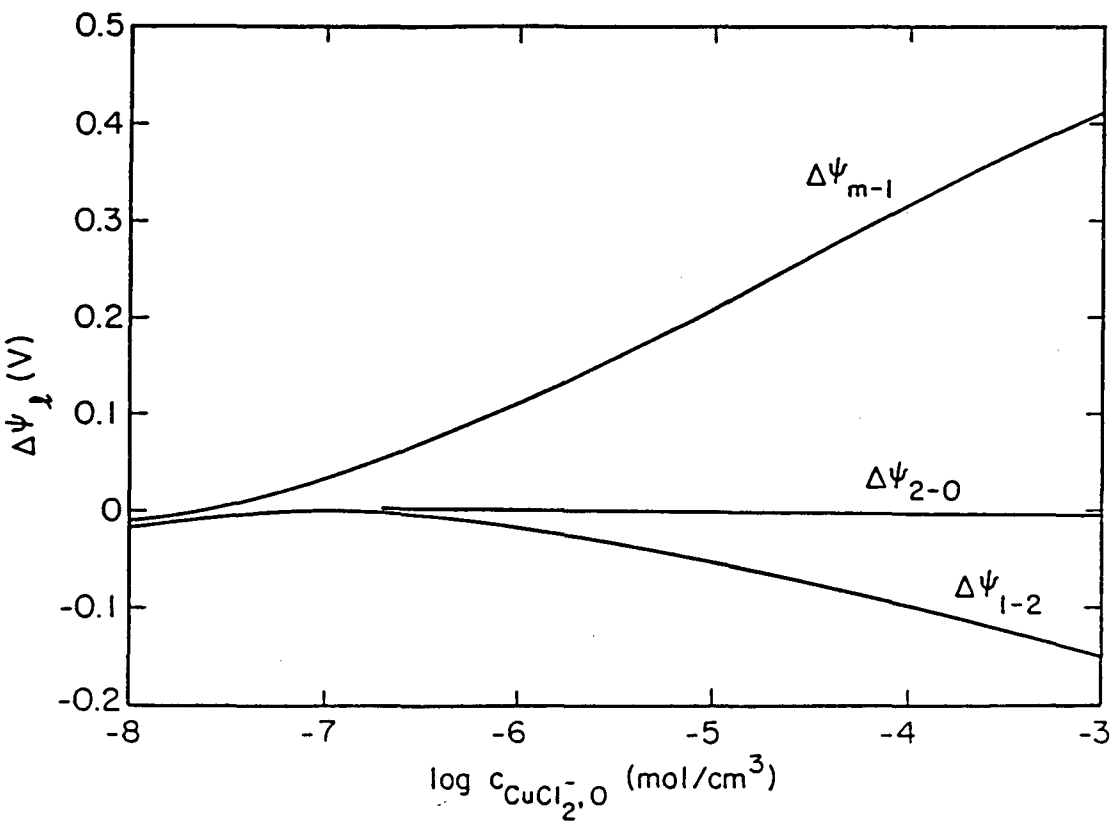

Figure 7. Equilibrated-interfacial potential-distribution map.

for, the concentration and potential dependent kinetic expressions given earlier should be utilized in conjunction with Gauss's law and the transport equations. The details of characterizing these interactions quantitatively were described in reference [3].

The only parameters in the microscopic model remaining to be discussed are the electron-transfer and desorption/adsorption reaction kinetic constants. Selection of the backward rate constant $k_{b,l}$ for each charge-transfer reaction l is made using an iterative procedure, where the experimental impedance data[4] is used as a guide. Let us next discuss further the measured impedance results for the copper chloride system.

It is well known[11] that the copper dissolution process is predominately mass-transfer controlled, but a contribution, possibly due to adsorption kinetics, can be identified by the frequency dependence of the measured complex impedance. In the high-frequency limit of figure 1, the slope is greater than a convective-diffusion 45° (Warburg) line. Thus, the adjustable rate constants are selected to account for the fast, but finite, rates of reaction.

A trial and error procedure is used to select a set of three equilibrium constants and three backward rate constants that when used in the microscopic impedance model yield simulated results that match the experimental data. The method is based on guessing a value for the surface coverage of adsorbed ions at the IHP, which enables the interfacial equilibrium constants to be determined analytically from simplified forms of the general equations described in the previous section. Moderately small coverages are selected so that the number of available sites on the surface do not limit the reactions. Relatively large values for the backward rate constants are then chosen, but must be iterated upon until numerical results give the desired steady-state current density and

impedance curves.

The set of equilibrium constants and kinetic parameters (backward rate constants and symmetry factors) used in the microscopic model are summarized in table 4. The forward rate constants $k_{f,l}$ also are given for completeness, but they are not independent adjustable parameters. The microscopic-model parameters are based on a surface coverage of $\Theta_i = 10^{-3}$, but it should be pointed out that the impedance simulations are sensitive to this parameter (values of 10^{-1} and 10^{-2} were tried before getting the desired results). This coverage, when used in equation 20, yields a value for the macroscopic double-layer capacity of $C_{dl} = 6\ \mu\text{F}/\text{cm}^2$.

Also given in table 4 are the equilibrium constant K_c and backward rate constant k_c' used in mechanism I. These parameters were reported elsewhere[5],[6] to describe the copper dissolution process in 0.1 N HCl and have not been adjusted. The symmetry factors β_l are not varied in either mechanism.

Table 4. Kinetic parameters for the charge-transfer reactions in mechanisms I and II.

reaction l	Equilibrium Constant K_l	Rate Constants Forward $k_{f,l}$	Rate Constants Back $k_{b,l}$	Symmetry Factor β_l
I. 1	10^4 cm^3/mol	10^3 cm^4/mol·s	10^{-1} cm/s	½
II. 1	9.98×10^{-2} mol/cm^3	9.98×10^7 1/s	10^9 cm^3/mol·s	½
II. 2	4.71×10^2	1.41×10^6 cm^4/mol^2·s	3×10^3 cm^4/mol^2·s	½
II. 3	3.39×10^{-5} mol/cm^3	3.39×10^4 1/s	10^9 cm^3/mol·s	½

4. Results

Results of the macroscopic and microscopic impedance models are to be presented for the largely mass-transfer controlled anodic dissolution of copper in 0.1 M HCl.[4] This system is a good test case for the purpose of exploring and providing an understanding of the nature of the interface, since slow reaction kinetics do not dictate or complicate the impedance response. Macroscopic impedance results are given first followed by the microscopic model results.

The electrochemical impedance for a copper disk rotating at 2000 rpm in 0.1 N hydrochloric acid is calculated by the macroscopic model based on the overall dissolution reaction (equation 1). The resulting electrode frequency response (at $V = -0.205$ V) is plotted in the complex plane in figure 8 based on a constant double layer capacity. Total impedance results for three different values of C_{dl} (5, 10, and 30 μF/cm^2) are illustrated on this Nyquist plot showing the negative of the imaginary part of the impedance *versus* the real part of Z with the frequency as a parameter. In addition to the total impedance, the faradaic and solution impedances are shown in figure 8, denoted by dashed and dotted lines, respectively. Let us now discuss further the components of Z_{tot}.

The faradaic impedance was defined earlier so that it includes not only the effect of the faradaic charge-transfer reactions but also that of any concentration variations at the electrode surface that affect the rate of the electrochemical reactions. Because the reaction is fast, the 45° line, or Warburg diffusion impedance, dominates the faradaic impedance since the charge-transfer resistance is small. Thus, these mass-transfer effects are characterized by the second term on the right of equation 9, the convective-

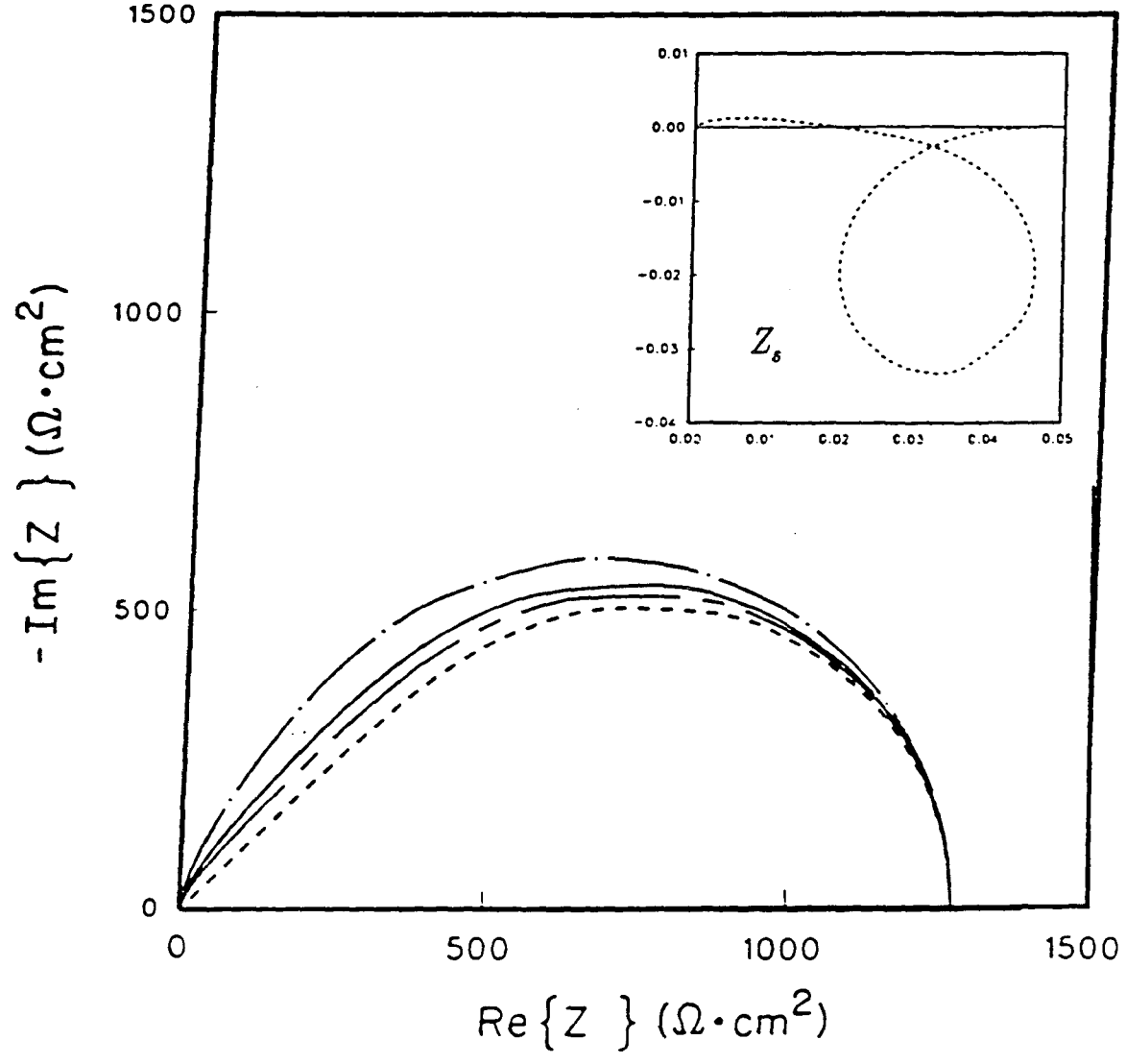

Figure 8. Complex-plane plot of the impedance for the anodic dissolution of copper as calculated by the Stefan-Maxwell macroscopic model based on mechanism I. Simulations of the total ($C_{dl} = 10$ μF/cm^2), faradaic, and solution impedances are denoted by solid, dashed and dotted lines, respectively. The total impedance based on $C_{dl} =$ 5 and 30 μF/cm^2 also are given by chain-dashed and chain-dotted lines, respectively.

Warburg impedance. The high-frequency limit of Z_f is given by $R_t = \lim_{\omega \to \infty} \{Z_f\}$, but is negligible on the scale of figure 8, again because reaction 1 is fast. The polarization resistance, the low-frequency limit of the faradaic impedance $R_p = \lim_{\omega \to 0} \{Z_f\} = R_t + R_0$ $= 1272\ \Omega \cdot \mathrm{cm}^2$, reduces to the mass-transfer resistance R_0. The faradaic impedance is characterized by R_0 and the convective-diffusion time constant τ_{MT}. $\tau_{MT} \propto Sc^{1/3}/\Omega$ is a function of the rotation speed Ω and the Schmidt number $Sc = \nu/D_i$, where Sc is based on the kinematic viscosity ν and the diffusion coefficient of the minor ($CuCl_2^-$) species.

The solution impedance arises from the potential difference across the diffusion layer. Although Z_{soln} is negligible for the conditions reported here, the inductive loop that appears near the origin is interesting and therefore is illustrated in the expanded view in figure 8. This feature in the solution impedance arises from the maximum that occurs in the steady-state potential profile,[12] which results from the diffusion potential balancing the potential as given by Ohm's law. This behavior, where the electric field in the solution is reversed, has been shown[13] to occur for a number of different electrochemical systems.

The total impedance calculated using the base-case capacitance value of $10\ \mu\mathrm{F/cm}^2$ (solid curve in figure 8) consists of one loop because the electrochemical reaction is fast (the charge-transfer resistance is negligible on the scale of the figure), and therefore an additional inner (high frequency) heterogeneous-reaction loop is not observed next to the low-frequency convective-Warburg impedance. Instead, the impedance resulting from the double-layer capacity simply shifts the frequency

dependence of the dominant mass-transfer (Warburg) impedance due to the overlapping capacitive time constant. The net effect is a high-frequency slope greater than 45° - the expected result for a convective-diffusion impedance. The solution resistance R_Ω is the high frequency limit of Z_{tot} because the time scale is so short that other effects cannot manifest themselves as factors influencing the current. However, R_Ω also is negligible relative to the polarization resistance.

The total impedance based on $C_{dl} = 5$ and 30 μF/cm^2 are also given in figure 8 by chain-dashed and chain-dotted curves, respectively. As $C_{dl} \rightarrow 0$, the total impedance reduces to the faradaic impedance, since

$$Z'_{tot} = \left[\frac{1}{Z_f} + j\omega C_{dl}\right]^{-1} + R_\Omega \quad . \tag{25}$$

Equation 25 is obtained from the more general total impedance equation 8 by assuming that the solution potential is negligible and that $\tilde{i}_c = j\omega C_{dl}\tilde{V}$.

For larger values of C_{dl}, the impedance spectra in the complex plane approaches a semicircle. The frequency $\omega_{max} = 2\pi f_{max}$ associated with the maximum in the imaginary part of the total impedance can be related to the time constant $\tau = 1/\omega_{max}$. Because the solution and charge-transfer resistances are small, the kinetic time constant, $\tau = (R_\Omega + R_t)C_{dl}$, is not important. Instead, the total impedance is characterized by $\tau = (R_\Omega + R_p)C_{dl}$, where the magnitude of the impedance loop is determined by the mass-transfer resistance R_0 since $R_\Omega + R_p \approx R_\Omega + R_0$. The characteristic dimensionless frequency at the impedance maximum of the total impedance ($C_{dl} = 30$ μF/cm^2) loop is $K_{max} = 1.6$, whereas $K_{max} = 3$ for the faradaic-impedance loop with no parallel capacitance.

Finally, it should be noted that the spacing of the frequencies on the complex-plane plot are highly nonuniform and visual interpolation can be difficult. Therefore, the same results given by figure 8 are presented next in the form of a Bode plot.

The total, faradaic, and solution impedances are presented in figure 9, where the logarithm of the magnitude of the impedance is plotted *vs.* the logarithm of the dimensionless frequency K. One advantage of the Bode plot is that the high frequency limit of the faradaic impedance, denoted by a dashed line, yields the charge-transfer resistance, a horizontal line at $\lim_{K \to \infty} \log|Z_f| = \log|R_t| = 0.158$, with a phase angle of 0° (although not shown); the complex-plane plot (figure 8) failed to provide $R_t = 1.44\ \Omega{\cdot}\mathrm{cm}^2$ quantitatively. The low-frequency limit of the faradaic impedance again yields the polarization resistance $R_p = 1272\ \Omega{\cdot}\mathrm{cm}^2$. In the intermediate high-to-moderate frequency range, the Warburg impedance is a straight line with a slope of $-1/2$ and a phase angle of -45°. An equivalent circuit model of the convective diffusion process is a transmission line[14] made up of a series of resistors and capacitors. Therefore, the corner frequencies of the faradaic impedance are not related to individual resistors and a capacitance.

The magnitude of the solution impedance is given by an almost horizontal line, on the scale of the figure, at $\lim_{K \to \infty} \log|Z_{soln}| = \log|R_\Omega| = 0.932$. An enlargement of Z_{soln} is included. This unexpected behavior on the Bode plot can be explained by the same reasoning as given earlier when Z_{soln} in the complex plane was discussed.

The total impedance for the base-case capacitance value of $10\ \mu\mathrm{F}/\mathrm{cm}^2$ is given by the solid line. The high-frequency limit is a horizontal line corresponding to

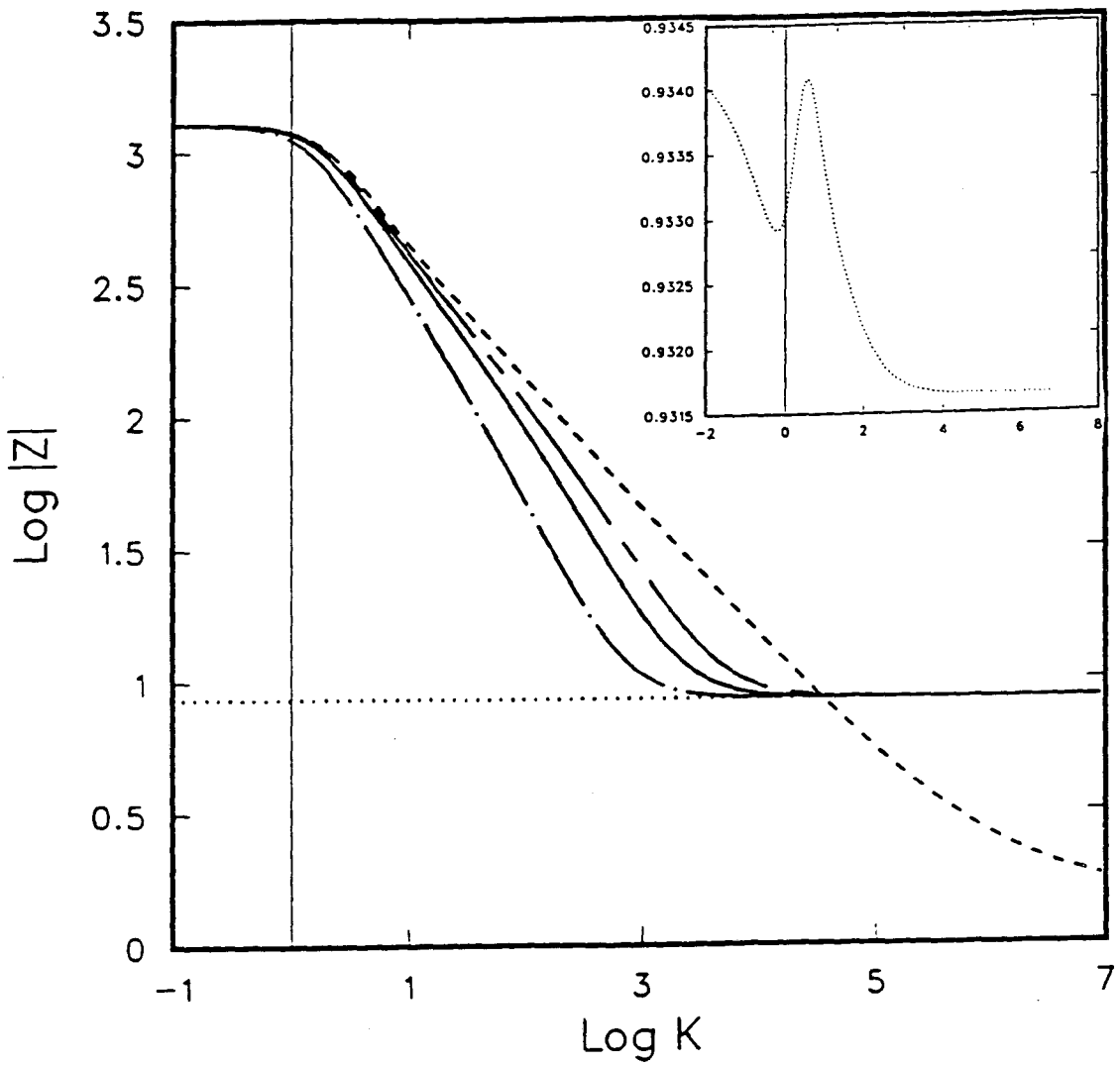

Figure 9. Bode plot of the total ($C_{dl} = 10\ \mu F/cm^2$), faradaic, and solution impedances for copper dissolution. The S-M simulations are based on mechanism I and are denoted by solid, dashed and dotted lines, respectively. The total impedance based on $C_{dl} =$ 5 and 30 $\mu F/cm^2$ are given by chain-dashed and chain-dotted lines, respectively.

$\lim_{K \to \infty} \{Z_{tot}\} = 8.544\ \Omega \cdot \mathrm{cm}^2$, and the low-frequency limit yields $R_p + \lim_{K \to 0} \{Z_{soln}\}$ $= 1281\ \Omega \cdot \mathrm{cm}^2$. The impedance of a "perfect capacitance" is represented as a straight line with a slope of -1 and a phase angle of $-90°$. The high-to-moderate frequency range of Z_{tot} corresponds to capacitive-like behavior. At lower frequencies, the slope shifts toward $-1/2$. The corner frequencies should be characterized by $\tau^{(HF)} = R_\Omega C_{dl}$ and $\tau^{(LF)} \approx (R_\Omega + R_0) C_{dl}$ for the high and low frequency limits, respectively.

The total impedance based on $C_{dl} = 5$ and $30\ \mu\mathrm{F/cm}^2$ are also given on the Bode plot in figure 9 by chain-dashed and chain-dotted lines, respectively. As C_{dl} increases, the high-frequency corner point decreases, and the negative close-to-unity slope is maintained over a wider frequency range. Again, at lower frequencies, the slope shifts toward $-1/2$. The low-frequency corner point is less sensitive to the value of the capacitance.

Results from both the macroscopic and microscopic impedance models are illustrated on the complex-plane plot in figure 10. The total impedance as calculated by the Stefan-Maxwell model (dotted line) is again based on mechanism I and a constant $C_{dl} = 10\ \mu\mathrm{F/cm}^2$, whereas the impedance from the microscopic model (solid line) is based on mechanism II and a capacitance that depends on the charge in the compact and diffuse layers. The latter simulated result is based on a set of parameters obtained from using $\Theta_i = 10^{-3}$ for Cl^- and $CuCl_2^-$. In other words, an 0.2 % total surface coverage is the basis for the numerical calculation and yields impedance results, $Z_{tot}^{(\mu M)}$, with two distinct regions in the moderate-to-high frequency range. At high frequencies, the slope of the $Z_{tot}^{(\mu M)}$ (solid) curve in figure 10 is greater than one, similar to the

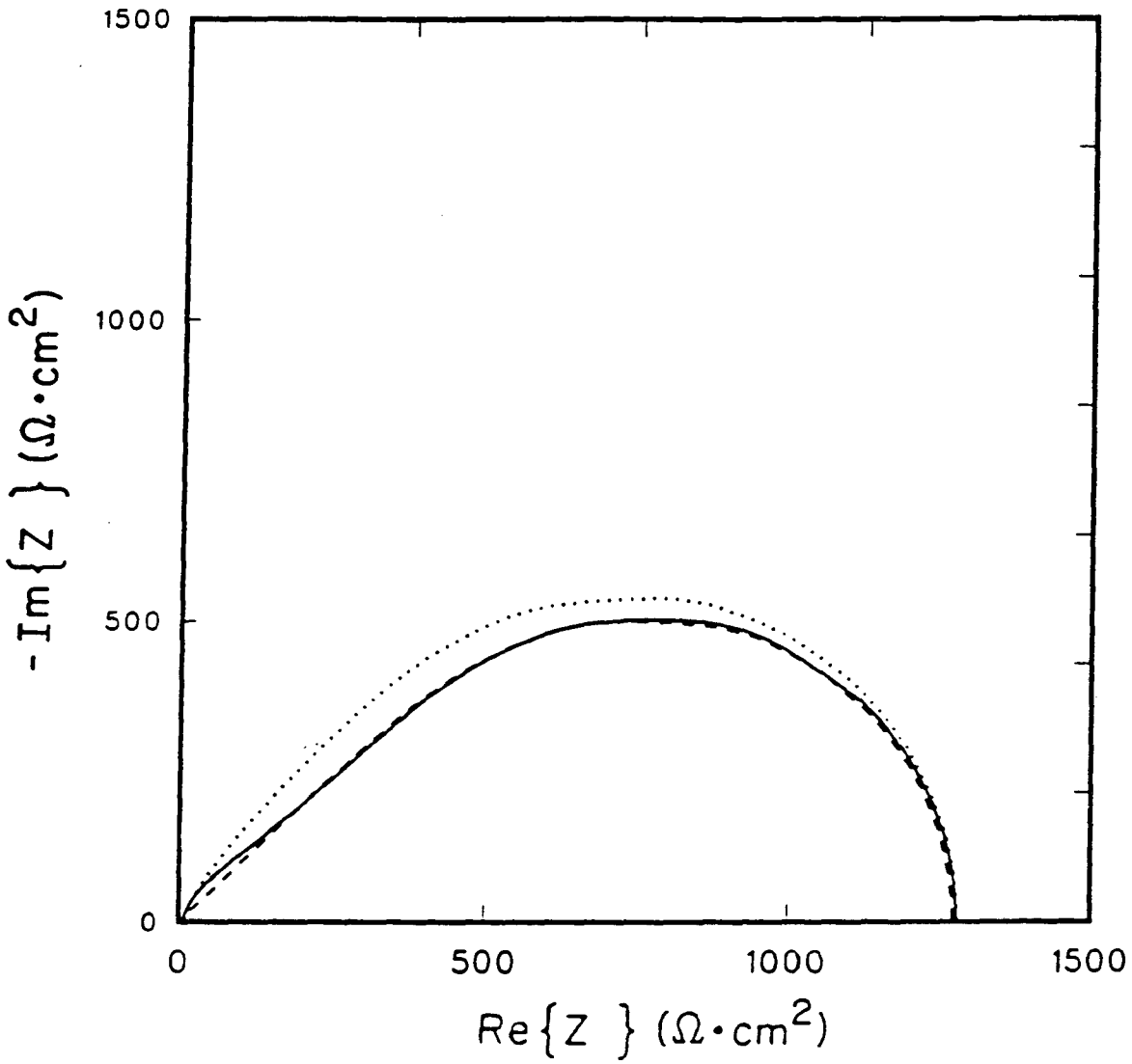

Figure 10. Complex-plane plot of the total impedance as calculated by the macroscopic and microscopic models based on mechanisms I (dotted line) and II (solid line), respectively. The Stefan-Maxwell faradaic impedance is denoted by a dashed line.

impedance results in figure 1.† The effective capacitance of the impedance appears to be close to 10 μF/cm^2, whereas at lower frequencies, the impedance becomes mass-transfer controlled, and the effective capacitance decreases. In all but the high-frequency limit, $Z_{tot}^{(\mu M)}$ corresponds to the Stefan-Maxwell faradaic impedance (dashed line). Thus, the macroscopic model yields reasonably accurate simulated results, but the microscopic model is necessary to yield a detailed and quantitative description of double-layer adsorption effects.

The total and faradaic impedances as calculated by the Stefan-Maxwell model using mechanism I are denoted in figure 11 by dotted and dashed lines, respectively. These results were presented in Bode form in figure 9 and are included here for comparison purposes only. Therefore, they will not be discussed further. The total microscopic impedance, based on mechanism II, but for a different set of rate constants, is given by a chain-dotted line in the figure. This set of parameters [to be described below] is denoted mechanism II (b); whereas, the set described earlier (table 4) [and denoted mechanism II (a)] is taken to be the base case and is given by a solid line in the figure. Simulations based on a new set of parameters are included to illustrate the importance and influence of the kinetic rate constants.

The microscopic kinetic-rate constants were chosen such that the low-frequency limits approximate the macroscopic model results. Values of 1279 and 1286 $\Omega \cdot$cm^2 are

† An alternative explanation has been given for why the experimental high-frequency data deviate from convective-Warburg behavior (and an expected slope of one). In reference [5], reaction 1 is treated as an EC reaction mechanism, and finite rates of the following homogeneous complexing reaction give rise to an additional impedance loop. For a large value of the chemical reaction rate constant, this can yield a high-frequency shoulder in the complex plane with a slope greater than one.

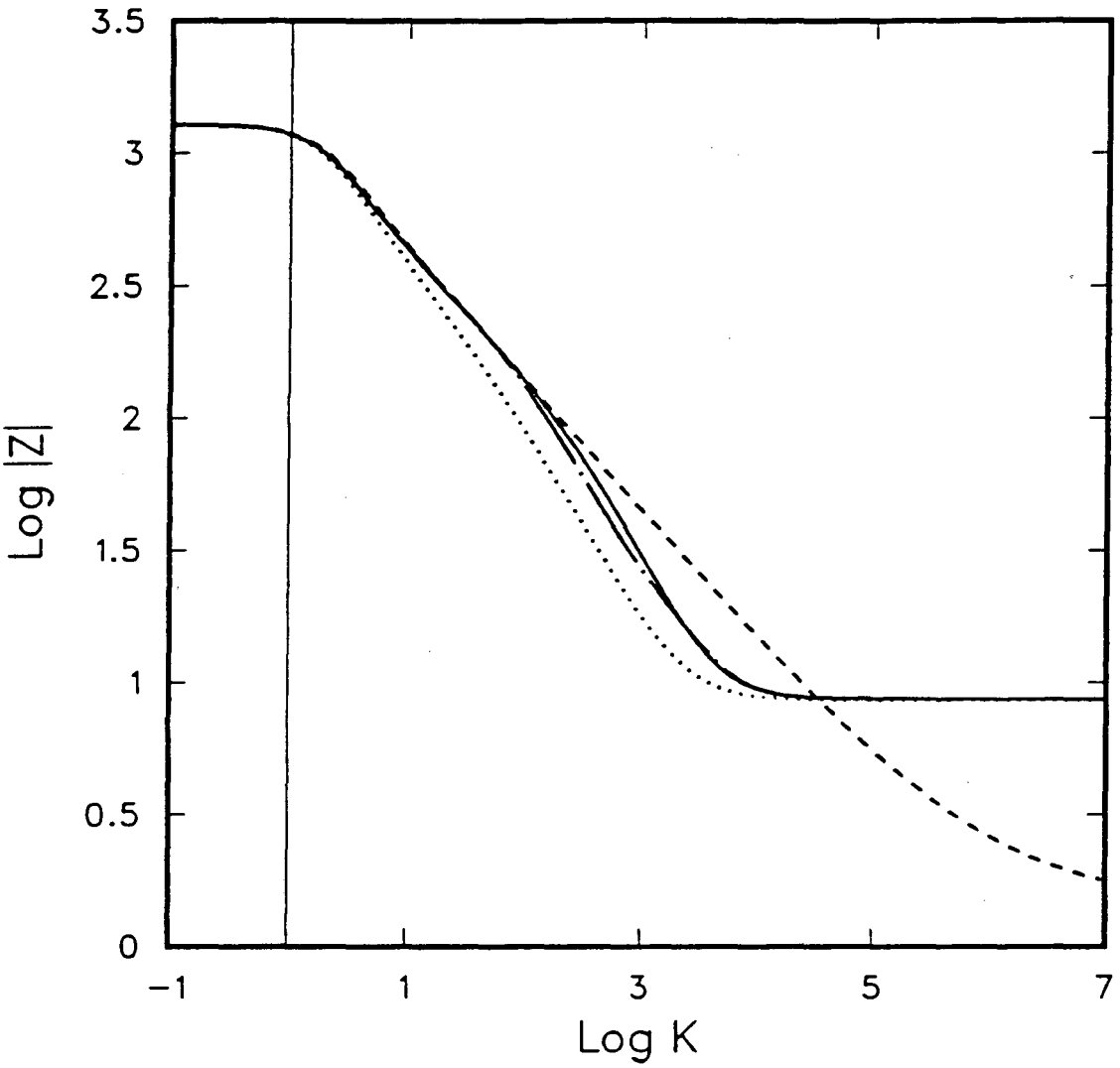

Figure 11. Bode plot of the total impedance as calculated by the microscopic model based on mechanisms II (a) and (b) and denoted by solid and chain-dotted lines, respectively. The Stefan-Maxwell total and faradaic impedances also are given and are denoted by dotted and dashed lines, respectively.

obtained for mechanisms II (a) and (b), respectively, which should be compared to the Stefan-Maxwell result, $R_\Omega + R_p = 1281\ \Omega\cdot\text{cm}^2$. The high-frequency limit yields quantitatively the solution resistance, $R_\Omega = 8.6652\ \Omega\cdot\text{cm}^2$, differing slightly (1.4%) from the Stefan-Maxwell result given earlier because the latter accounts for the diffusion potential and variation of conductivity. The intermediate frequency range of the microscopic impedance results has two distinguishing regions, as was also seen on the previous complex-plane plot. At moderate-to-high frequencies, Z_t has a slope close to -1 similar to Stefan-Maxwell total impedance and an effective capacitance that corresponds to $C_e = 5\ \mu\text{F}/\text{cm}^2$. At moderate-to-low frequencies, the slope shifts to a value of $-1/2$ indicating the importance of mass-transfer effects, and the effective capacitance decreases.

The total impedance curve denoted mechanism II (b) is based on the following set of rate constants for reactions 2 to 5: $k_b = 10^8$ $\text{cm}^3/\text{mol}\cdot\text{s}$, 5×10^3 1/s, and 10^8 $\text{cm}^3/\text{mol}\cdot\text{s}$, respectively. On figure 11, the frequency dependence of the transition from dominating mass-transfer effects to adsorption-kinetic control shifts due to the change in the adsorption reaction resistance. Decreasing the adsorption rate constant (larger R_a), as has been done for mechanism II (b), causes the slope to shift from $-1/2$ at a slightly lower frequency. In other words, faster adsorption rates cause the effective capacitance to become significant only at a slightly higher frequency.

Next, we should examine the microscopic impedance results in more detail. The total, electron-transfer, and desorption/adsorption impedances are shown in figure 12 for mechanism II (b). Z_{e^-} and Z_a are denoted by dashed and dotted lines, respectively. $Z_{tot}^{(\mu M)}$ should be compared to the total impedance in figure 8 obtained for mechanism II.

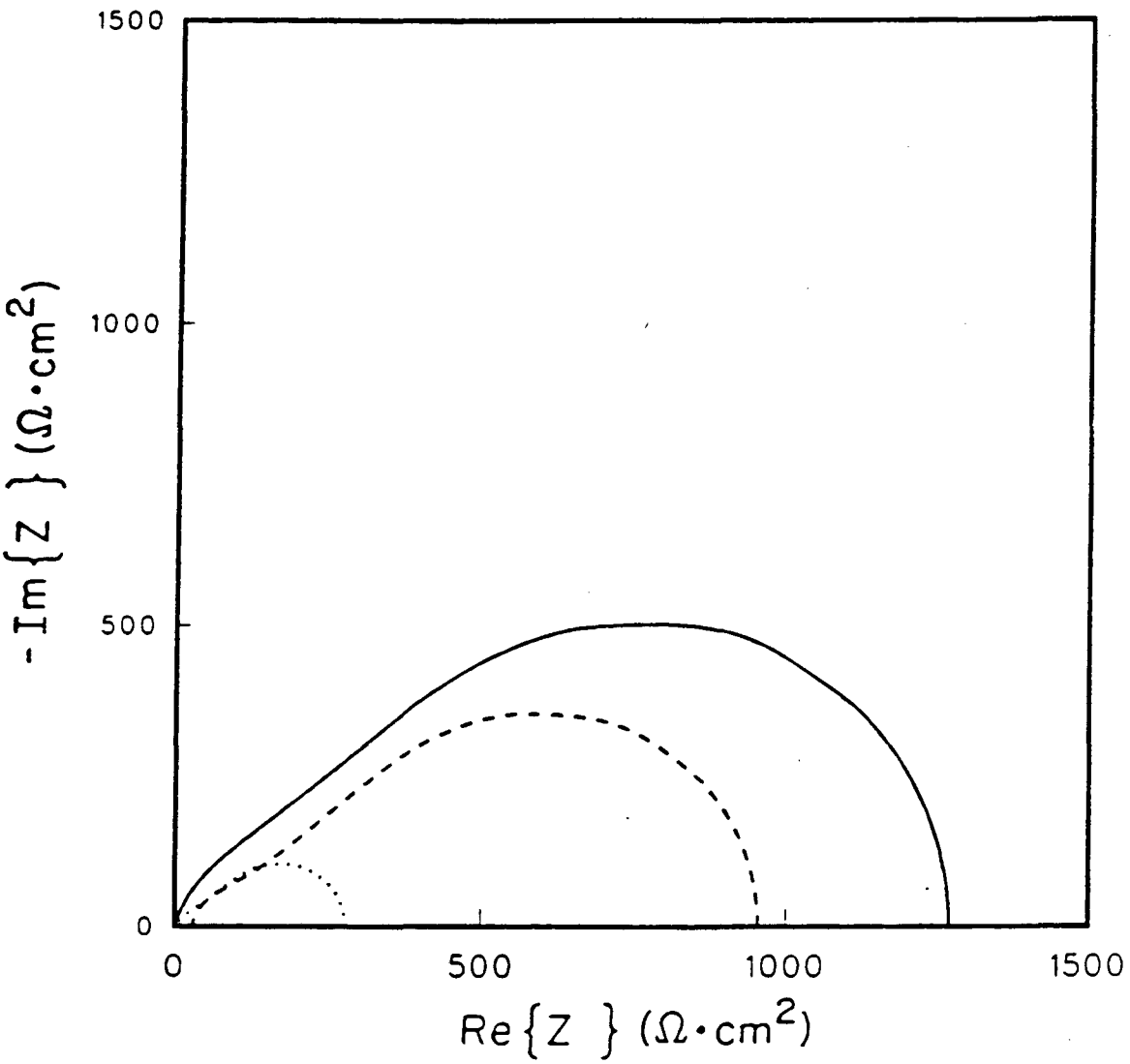

Figure 12. Complex-plane plot of the total, electron-transfer, and adsorption impedances as calculated by the microscopic model based on mechanism II (b) and denoted by solid, dashed, and dotted lines, respectively.

The different combination of parameters yields similar total impedance results, although the individual Z_{e^-} and Z_a components are different. However, until more measurements are carried out to confirm the existence of two different slopes in the moderate-to-high frequency range on the complex impedance plane, we cannot conclude which is the best set of parameters. Instead, we have demonstrated how to account for the proper concentration and potential dependence of the capacitance and have given results illustrating the frequency dispersion effect of the double-layer capacity.

5. Discussion of Results

Previously,[5] we discussed the use of the ac-impedance method for electrochemically measuring the rates of homogeneous reactions taking place in the solution. Here, we postulate an extension of that procedure, although results are not given. Frequently, homogeneous reactions are fast so that the reaction is taken to be equilibrated in the diffusion layer. However, finite rates of the chemical reaction must be accounted for in a thin reaction zone adjacent to the electrode surface. The thickness of the reaction layer is often comparable to that of the diffuse double layer, and rather complicated corrections then have to be carried out to allow for the variation in concentration and for the effect of the double-layer electric field on the transport of ions to the electrode. The microscopic model that has been used here is capable of investigating these complex interactions where electron-transfer, desorption/adsorption, finite rates of the homogeneous reaction, and diffusion and ohmic losses are all coupled. Finally, the microscopic model can be used for proposing different complex reaction mechanisms and predicting the resulting frequency dependence of the total impedance.

6. Conclusions

Results of two mathematical models have been presented. Both theoretical frameworks are used to determine the total impedance resulting from the current response (charge transfer and double-layer charging) to potential variations in the working electrode relative to a reference electrode placed in the bulk solution. The electrochemical impedance has been analyzed by examining each contribution of the total cell potential and current, which yielded impedance terms typically neglected in other ac-impedance treatments. Although, double-layer and transport phenomena are accounted for in both models, the emphasis of each algorithm is quite different; interfacial desorption/adsorption reactions coupled with electron-transfer reactions are the focus of the microscopic model, whereas transport in the diffusion layer and overall faradaic reactions are emphasized in the macroscopic model. Concentrated-solution theory, accounting for migration, convection, and multicomponent diffusion, is utilized in the Stefan-Maxwell program, whereas a simple dilute-solution Warburg diffusion layer is applied in the microscopic model.

A measure of the validity of the models can be obtained by comparison to experimental data. In this paper, we have used the macroscopic and microscopic models to study the largely mass-transfer controlled copper dissolution process in 0.1 M HCl. At the higher frequencies, the slope of a convective-diffusion (Warburg) impedance is expected to be 45°, but the impedance measurements given in figure 1 show a larger than 45° slope. The macroscopic-impedance model simulations, based on an overall dissolution reaction, predict this trend in the experimental data by accounting for a constant double-layer capacity, where the overlapping capacitive time constant distorts

(by increasing the slope of) the convective-diffusion 45° line. A refinement in the interpretation of the experimental data is that desorption/adsorption kinetic limitations can contribute to the steep high-frequency slope due to frequency dispersion of the double-layer capacity. The microscopic double-layer model accounts for a more detailed three-step (adsorption/charge-transfer/desorption) reaction mechanism having fast, but finite, rates of reaction. The later simulations yield an additional impedance loop in the high-frequency range, which (depending on the choice of surface coverage and rate constants) appear as a single loop with a larger than 45° Warburg slope.

There are many parameters in the microscopic model that characterize the double layer and cannot, in general, be independently measured. Thus, a detailed description of the equilibrated interface was given, which included surface-coverage and potential distribution maps as a function of supporting electrolyte concentration. Additionally, an iterative procedure for selecting equilibrium constants and kinetic rate constants has been discussed. The results of these procedures can be used to gain insight into the importance and influence of these parameters. Only a small number of carefully selected sets of parameters yielded quantitative agreement with the experimental data. Future experiments can be designed to further characterize the copper system and to verify the applicability of the mathematical models. Finally, the two models together provide a powerful arsenal for characterizing the total electrochemical impedance of many systems.

Acknowledgements

This work was supported by the Assistant Secretary for Conservation and Renewable Energy, Office of Energy Storage and Distribution, Energy Storage Division, of the U.S. Department of Energy under Contract No. DE—AC03—76SF00098.

List of Symbols

$c_{i,0}$	concentration of species i just outside the diffuse layer, mol/cm^3
$c_{i,\infty}$	concentration of species i in the bulk solution, mol/cm^3
C_{dl}	overall double-layer capacity used in the macroscopic model, F/cm^2
C_e	effective double-layer capacity, F/cm^2
C_j	capacity of region j used in the microscopic model, F/cm^2
C_{M-1}	capacity of region between the metal and the inner Helmholtz plane, F/cm^2
C_{1-2}	capacity of region between the inner and outer Helmholtz planes, F/cm^2
C_2	capacity of region between the outer Helmholtz plane and the outer limit of the diffuse layer, F/cm^2
d_{M-1}	distance between metal surface and the inner Helmholtz plane, cm
d_{1-2}	distance between the inner Helmholtz plane and the outer Helmholtz plane, cm
D_i	diffusion coefficient of species i, cm^2/s
e^-	symbol for the electron
f	frequency, Hz
F	Faraday's constant, 96,487 C/equiv
i	total current density, A/cm^2
i_a	current density of desorption/adsorption reaction l, A/cm^2
i_c	capacitive current density, A/cm^2

i_{e^-}	current density of electron-transfer reaction l, A/cm^2
i_f	current density of faradaic reaction l, A/cm^2
$\tilde{i}$	alternating current density, A/cm^2
j	$=\sqrt{-1}$ imaginary number
k_a', k_c'	anodic and cathodic rate constant for a charge transfer reaction in the macroscopic model
k_f, k_b	forward and back rate constants for an desorption/adsorption reaction in the microscopic model
K	dimensionless frequency
K_l	equilibrium constant
n_l	number of electrons involved in electrode reaction l
q	surface charge density on the metal side of the double layer, C/cm^2
q_1	surface charge density at the inner Helmholtz plane, C/cm^2
q_2	surface charge density in the diffuse part of the double layer, C/cm^2
r_l	rate of charge-transfer reaction l, mol/cm^2-s
r_0	radius of disk, cm
R	universal gas constant, 8.3143 J/mol-K
R_Ω	primary solution resistance, ohm·cm^2
$s_{i,l}$	stoichiometric coefficient of species i in electrode reaction l
Sc	Schmidt number
T	absolute temperature, K
u_i	mobility of species i, cm^2·mol/J·s

V	kinetic potential difference (electrode potential relative to given reference electrode placed just outside the diffuse layer), V
V_{tot}	total potential (electrode potential relative to given reference electrode placed in the bulk solution), V
$\widetilde{V}_{tot}$	total alternating potential (electrode potential relative to given reference electrode placed in the bulk solution), V
$\widetilde{V}$	alternating kinetic potential difference (electrode potential relative to given reference electrode placed just outside the diffuse layer), V
z_i	charge number of species i
Z_a	complex adsorption impedance, ohm·cm^2
Z_{e^-}	complex electron-transfer impedance, ohm·cm^2
Z_f	complex faradaic impedance, ohm·cm^2
Z_s	complex solution impedance, ohm·cm^2
Z_{tot}	complex total impedance, ohm·cm^2
Z'_{tot}	equivalent circuit approximation for the complex total impedance, ohm·cm^2

Greek symbols:

β_l	transfer coefficient of reaction l
$\Gamma_{i,1}$	surface concentration of species i at the IHP, mol/cm^2
$\Gamma_{i,d}$	surface concentration of species i in the diffuse layer, mol/cm^2
Γ_{max}	maximum number of active surface sites, mol/cm^2
$\Delta\Gamma$	available surface sites, mol/cm^2
δ_i	scaling factor for the diffusion layer of species i, cm
$\overline{\delta}$	Nernst diffusion layer thickness, cm

ϵ_j	permittivity of region j, F/cm or C/V-cm
$\Delta\psi_{M-1}$	cavity potential difference between electrode and inner Helmholtz plane, V
$\Delta\psi_{1-2}$	cavity potential difference between inner and outer Helmholtz planes, V
$\Delta\psi_{2-0}$	cavity potential difference across the diffuse layer, V
$\Delta\psi_{IR}$	ohmic cavity potential difference, V
$\Delta\psi_{diff}$	cavity diffusion potential, V
$\Delta\psi_{ref}$	cavity reference potential difference, V
$-1/\theta'(0)$	dimensionless Warburg impedance function
Θ_i	surface coverage of species i
κ_∞	conductivity of the bulk solution, ohm^{-1}-cm^{-1}
λ	Debye length, cm
ν	kinematic viscosity, cm^2/s
ξ	dimensionless axial distance for rotating-disk convective-diffusion equation
π	3.141592654
τ	time constant, s
Φ_m	electric potential of the metal electrode, V
Φ_{RR}	potential of a real reference electrode placed in the bulk solution, V
Φ_0	potential of a hypothetical reference electrode of a given kind placed just outside the diffuse layer, V
$\hat{\Phi}_0$	potential of a hypothetical reference electrode of a given kind placed just outside the diffuse layer as if there were no concentration gradients across the boundary layer, V

$\tilde{\Phi}_0$	alternating potential of a hypothetical reference electrode of a given kind placed just outside the diffuse layer, V
$\tilde{\bar{\Phi}}_0$	alternating potential of a hypothetical reference electrode of a given kind placed just outside the diffuse layer as if there were no concentration gradients across the boundary layer, V
ω	perturbation frequency, rad/s
ω_{max}	frequency characteristic of the maximum of an impedance loop, rad/s
Ω	angular rotation speed, rad/s
subscripts:	
m	at the metal electrode surface
0	just outside the diffuse part of the double layer
∞	in the bulk electrolyte, where there are no concentration variations
1	at the inner Helmholtz plane
2	at the outer Helmholtz plane
superscripts:	
(M-1)	between metal and IHP
(1-2)	between IHP and OHP
(2)	between OHP and outer limit of diffuse layer
(IHP)	at the inner Helmholtz plane
(OHP)	at the outer Helmholtz plane
~	complex part

References

[1]. Alan K. Hauser and John Newman, "A Macroscopic-Impedance Model for a Rotating-Disk Electrode," LBL-26267, submitted to the *Journal of the Electrochemical Society (1989).*

[2]. David C. Grahame, "Mathematical Theory of the Faradaic Admittance (Pseudocapacity and Polarization Resistance)," *Journal of the Electrochemical Society, 99,* 370C-385C (1952).

[3]. Alan K. Hauser and John Newman, "A Microscopic-Impedance Model for a Rotating Disk," LBL-26268, submitted to the *Journal of the Electrochemical Society (1989).*

[4]. William H. Smyrl, "Digital Impedance for Faradaic Analysis. II. Electrodissolution of Cu in HCl," *Journal of the Electrochemical Society, 132,* 1555-1562 (1984).

[5]. Alan K. Hauser and John Newman, "Singular Perturbation Analysis of the Faradaic Impedance of Copper Dissolution Accounting for the Effects of Finite Rates of a Homogeneous Reaction," LBL-25706, submitted to the *Journal of the Electrochemical Society* (1988).

[6]. Alan K. Hauser and John Newman, "The Effect of Schmidt Number on the Faradaic Impedance of the Dissolution of Copper Disk," LBL-25721, submitted to the *Journal of the Electrochemical Society* (1988).

[7]. John Newman, "Resistance for Flow of Current to a Disk," *Journal of the Electrochemical Society, 113,* 501-502 (1966).

[8]. Bernard Tribollet and John Newman, "Analytic Expression of the Warburg Impedance for a Rotating Disk Electrode," *Journal of the Electrochemical Society, 130,* 822-824 (1983).

[9]. John Newman, *Electrochemical Systems,* Englewood Cliffs, N. J.: Prentice-Hall, Inc., 1973.

[10]. R. A. Robinson and R. H. Stokes, *Electrolyte Solutions,* London: Butterworths, 1965.

[11]. William H. Smyrl, "Electrochemistry and Corrosion on Homogeneous and Heterogeneous Metal Surfaces," *Comprehensive Treatise of Electrochemistry, 4,* Chapter 2, J. O'M. Bockris, Brian E. Conway, Ernest Yeager, and Ralph E. White, eds., New York: Plenum Publishing Corporation, 1981, pp. 97-149.

[12]. Alan K. Hauser and John Newman, "Potential and Concentration Variations of the Reacting, Supporting Electrolyte," LBL-25608, submitted to the *Journal of the Electrochemical Society* (1988).

[13]. Alan K. Hauser and John Newman, "Electrolytic Mass Transfer to a Rotating Disk in Dilute Solutions: Concentration Variations of the Reacting, Excessive Supporting Electrolyte," Abstract 545, Spring ECS Meeting, Atlanta, 1988.

[14]. *Impedance Spectroscopy—Emphasizing Solid Materials and Systems,* J. Ross Macdonald, ed., New York: John Wiley & Sons, 1987.

LAWRENCE BERKELEY LABORATORY
TECHNICAL INFORMATION DEPARTMENT
1 CYCLOTRON ROAD
BERKELEY, CALIFORNIA 94720